Journal of the European Ceramic Society 41 (2021) 6660–6669

Contents lists available at ScienceDirect

Journal of the European Ceramic Society

journal homepage: www.elsevier.com/locate/jeurceramsoc

Hidden transformations in entropy-stabilized oxides

Alexander D. Dupuy [a,*], I-Ting Chiu [b], Padraic Shafer [c], Elke Arenholz [d], Yayoi Takamura [e], Julie M. Schoenung [a]

[a] Department of Materials Science and Engineering, University of California, Irvine, Irvine, CA 92697, USA
[b] Department of Chemical Engineering, University of California, Davis, Davis, CA 95616, USA
[c] Advanced Light Source, Lawrence Berkeley National Laboratory, Berkeley, CA 94720, USA
[d] Cornell High Energy Synchrotron Source, Cornell University, Ithaca, NY 14853, USA
[e] Department of Materials Science and Engineering, University of California, Davis, Davis, CA 95616, USA

ARTICLE INFO

Keywords:
High entropy oxides (HEO)
X-ray absorption spectroscopy (XAS)
Phase transformation
Valence state
Coordination state

ABSTRACT

Entropy-stabilized oxides (ESO) display a reversible entropy-driven phase transformation that can be leveraged to produce a continuum of metastable phase states, allowing for property optimization and novel functionalities. X-ray absorption spectroscopy reveals that entropic stabilization extends to the electronic structure (valence state and cation coordination) in sintered (Co,Cu,Mg,Ni,Zn)O, manifesting as a tunable lattice distortion in the entropy-stabilized phase. Co, Cu, and Zn ions reversibly transform from six-fold to four-fold coordinated structures and from low to high valence states due to the competition between electronic structures that are equilibrium and enthalpy-driven or metastable and entropy-driven. The segregation of a Cu-rich tenorite phase and a Co-rich spinel phase influences the electronic structure evolution. ESOs can adjust their electronic structures through heat treatment, providing a powerful tool for developing functional properties. These results indicate that the definition of entropy stabilization should include entropy-stabilized electronic structures, providing motivation to reassess previously studied HEO materials.

1. Introduction

The creation of the single-phase solid solution (Co,Cu,Mg,Ni,Zn)O in 2015 led to the discovery of a new class of ceramics, referred to as high-entropy oxides (HEO) [1]. Since that time, HEOs have garnered attention for their ability to greatly expand the compositional space of ceramic materials. High entropy design concepts have been applied to oxide systems with different compositions and crystal structures [2]. HEOs are already showing promise as high performance functional materials for potential applications such as capacitors [3], electrolytes [4], catalysts [5], and cathodes [6].

A distinction should be made between materials that have high entropy and materials that are *entropy-stabilized*. Entropy will play a meaningful role in the thermodynamic stability of oxides when cation occupancy is random on a particular sublattice. However, the role of entropy on thermodynamic stability is heavily regulated by temperature, with the stable phase state being an outcome of a competition between entropy and enthalpy. An entropy-stabilized oxide (ESO) has a metastable entropy-driven single-phase state that outcompetes the free energy of the equilibrium enthalpy-driven multi-phase state. This metastability enables a *reversible* entropic phase transformation, giving rise to a continuum of phase heterogeneity that can be modified by heat treating within a specific temperature window. However, little is currently known about the phase transformation behavior in ESO materials, what mechanisms drive the transformations, and if those mechanisms are universal to all ESO materials. Instead, we refer to the transformation temperature window and controllable phase states resulting from the reversible entropic transformations inherent to ESO materials more generally as the "phase spectrum". Our previous work has shown that (Co,Cu,Mg,Ni,Zn)O manifests the phase spectrum by segregating a Cu-rich multi-component tenorite phase, the atomic percent (at%) of which can be controlled through heat treatment [7]. Although Cu is the majority cation, this tenorite secondary phase also contains significant amounts of the other four cations. The morphology and phase evolution of this tenorite phase is greatly influenced by the grain size of the sintered specimens. Access to the phase spectrum provides ESOs an unprecedented capacity for phase and microstructural engineering, enabling optimization of properties and the development

* Corresponding author.
E-mail address: dupuya@uci.edu (A.D. Dupuy).

https://doi.org/10.1016/j.jeurceramsoc.2021.06.014
Received 9 March 2021; Received in revised form 3 June 2021; Accepted 9 June 2021
Available online 11 June 2021

of new functionalities.

The entropy-stabilized phase state of (Co,Cu,Mg,Ni,Zn)O possesses a cubic rocksalt crystal structure with a complex cation coordination, exhibiting a Jahn-Teller distortion of the CuO_6 octahedron leading to asymmetric Cu-O bond lengths [8]. The distortion arises from a competition between the elongated coordination preferred by Cu ions and the regular octahedral coordination preferred by the other cations. By examining the full-width-at-half-maximum (FWHM) of the (Co,Cu,Mg,Ni,Zn)O rocksalt X-ray diffraction (XRD) peaks, Berardan et al. demonstrated that the lattice distortion in the rocksalt crystal structure can be modified through heat treatment, changing the functional properties [9]. These preliminary studies show that ESOs can form unique metastable electronic structures (valence state and cation coordination), possibly due to changes in the cation coordination behavior. The electronic structure plays a critical role in a wide range of functional properties, including but not limited to: magnetic, electronic, dielectric, electrochemical, electrocatalytic, and superconducting properties. Having a tunable electronic structure would allow optimization and potentially the realization of new functional properties in ESOs, greatly expanding their applications.

The influence of heat treatment and grain size on the lattice distortion within the crystal structure and electronic structure of ESO's is not well understood. Here we use X-ray absorption spectroscopy (XAS) on sintered (Co,Cu,Mg,Ni,Zn)O samples to show that an evolution in the lattice distortion of the rocksalt crystal structure occurs due to changes in the cation electronic structure with heat-treatment condition. The (Co,Cu,Mg,Ni,Zn)O composition was chosen because it is the most well studied ESO material and is known to exhibit interesting phase and structural transformation behavior in response to heat treatment, making it an ideal material to study how heat treatment will influence the electronic structure in ESO materials. Consolidation was performed using spark plasma sintering (SPS) and conventional sintering, allowing for nanocrystalline and coarse-grained samples to be prepared. Cu, Zn, and Co ions experience changes to their electronic structures after heat treatment, and the evolution differs between the coarse-grained and nanocrystalline samples. Changes in the electronic structures of Mg and Ni ions were not observed. Through heat treatment, the competition between entropy and enthalpy can drive the cations in ESO materials to do any combination of the following reversible behaviors: (1) segregate into a secondary phase, (2) change valence state, or (3) change local cation coordination environment. To explore these possibilities, we systematically consider the following, as described below: (a) the effect of grain size and heat-treatment conditions on phase state and microstructure using XRD, scanning electron microscopy (SEM), and energy dispersive X-ray spectroscopy (EDS); (b) the effect of the same on electronic structure (valence state and cation coordination) using XAS; and (c) the mechanisms that control these effects.

2. Experimental methods

2.1. Processing and synthesis

NiO (18 nm reported particle size, 99.98 wt% purity), MgO (50 nm, 99.95 %), ZnO (18 nm, 99.95 %), CuO (25−55 nm, 99.95 %), and CoO (50 nm, 99.7 %) nanopowders were blended in equimolar amounts, then milled at 300 rpm for 3 h using planetary ball milling (PBM) in a Fritsch Premium 7 ball mill. Milling was performed using silicon nitride jars and milling media with the powder suspended in isopropanol. These powders were used to consolidate coarse-grained samples using conventional sintering in a CM Furnaces 1210BL elevator furnace at 1100 °C for 24 h. The same powders were reacted at 900 °C for 20 min to form a homogeneous single phase. These single-phase powders were then milled using PBM at 300 rpm for 12 h and consolidated into nanocrystalline single-phase bulk samples using a Fuji model 825S SPS. The powders were sintered at 700 °C for 5 min using a heating rate of 200 °C/min and pressure of 100 MPa.

Heat treatments were performed using an elevator furnace at temperatures ranging from $T_{HT} = 500-850$ °C and hold times from 2 to 12 h. The hot zone of the furnace was first heated to the target temperature. The room temperature sample and elevator were then lifted into the hot zone, allowing the sample to heat rapidly and prevent the sample from spending time at lower temperatures that might convolute the phase state at the target temperature. Samples were quenched by lowering the elevator into the path of a fan blowing room temperature air. Further details about the synthesis, consolidation, and heat-treatment procedures can be found in our previous work [7].

2.2. Characterization

Average grain size was measured from fractured surfaces using a Hitachi Regulus 8230 SEM. Elemental mapping was performed on polished samples using a Bruker QUANTAX FlatQUAD EDS with a low accelerating voltage (3 kV), allowing for <100 nm features to be resolved [10]. The bulk phase state, i.e., values for X_T and X_S, was assessed with XRD using an Ultima III diffractometer and Rietveld refinement using MAUD [11]. XA spectra were collected at beamline 4.0.2 at the Advanced Light Source. Total electron yield (TEY) detection mode was used with the X-ray beam incident upon the sample at 30° grazing incidence from the sample surface. Although the electron escape depth of TEY detection is limited to 5−10 nm in oxides [12], the samples were polished and cleaned before measurement to remove any surface specific features.

3. Results and discussion

3.1. Microstructure and phase state

As-consolidated grain size is controlled through sintering conditions. Conventional sintering at 1100 °C for 24 h produced coarse-grained samples with an average grain size of 16 μm and an equiaxed microstructure, seen in the SEM micrograph in Fig. 1a. Large grains arise due to the high temperatures and long hold times used in conventional sintering. In contrast, SPS consolidation at 700 °C for 5 min produced nanocrystalline samples with an average grain size of 98 nm (Fig. 1b), where minimal grain growth occurs due to the low temperatures and short times needed for densification. Both conventional sintering and SPS processed samples had relative densities >98 % in the as-sintered state.

Coarse-grained samples display a similar phase evolution to what was observed in our previous work [7]. As-sintered coarse-grained samples (labeled as CG-AS) and samples heat treated at T_{HT} =850 °C for 2 h (labeled CG-850C-2h) are single phase, and do not exhibit tenorite peaks in XRD because they are quenched from above the entropic phase transformation temperature (~850 °C) (Fig. 2a). A Cu-rich tenorite phase (XRD peaks labeled 'T' in Fig. 2a) emerges in sample CG-800C-2h, and the at% of this Cu-rich tenorite phase (X_T) increases as T_{HT} decreases until T_{HT} =700 °C. X_T increases with increasing heat-treatment time as well, reaching a maximum in sample CG-700C-12h ($X_T = 15.4$ at%). The Cu-rich phase is also observed by SEM and EDS, as shown for sample CG-700C-12h in Fig. 3a and b. It is important to note that the tenorite phase is multi-component and will contain the other four cations. Accordingly, a significant amount of Cu will remain in the rocksalt structure, even in sample CG-700C-12h (with $X_T = 16$ at%).

A third phase is also observed in the coarse-grained samples heat treated at T_{HT} =700 °C (XRD peaks labeled 'S' in Fig. 2a). These peaks correspond to a Co-rich spinel phase of the form MCo_2O_4 (where M = Cu, Mg, Ni, Zn). CoO is known to form spinel phases with all of the other metal ions in (Co,Cu,Mg,Ni,Zn)O [13]. Although spinel phases can form at a range of temperatures, only small amounts of spinel phase (X_S) are observed in a few of the coarse-grained samples, with $X_S = 5$ at% in CG-700C-2h, and $X_S = 10$ at% in CG-700C-12h. The presence of this Co-rich phase is also observed by EDS, as shown for sample

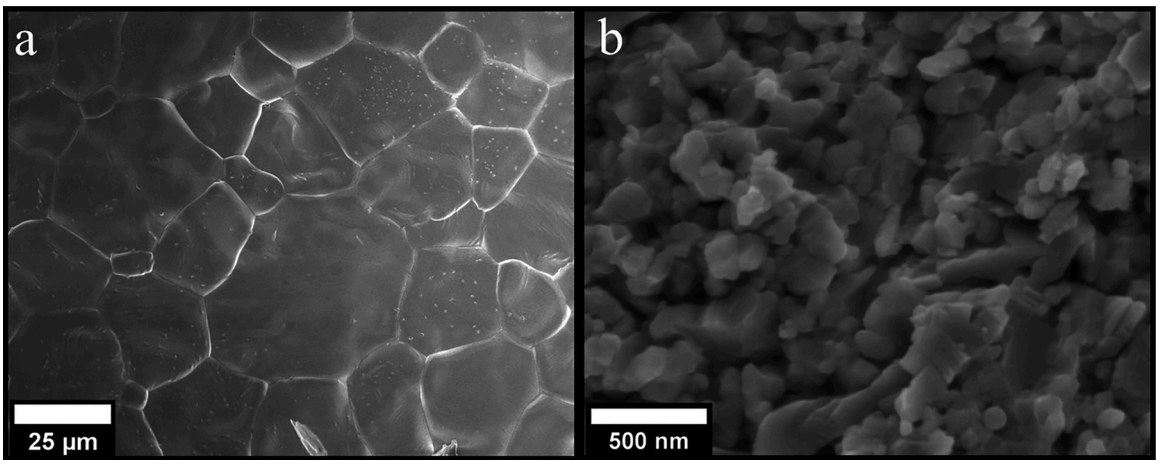

Fig. 1. Microstructures of the consolidated (Co,Cu,Mg,Ni,Zn)O samples. (a-b) Fracture surface micrographs of the (a) 1100 °C conventionally sintered, single-phase coarse-grained sample (CG-AS), and (b) 700 °C SPS consolidated, single-phase nanocrystalline sample (NC-AS).

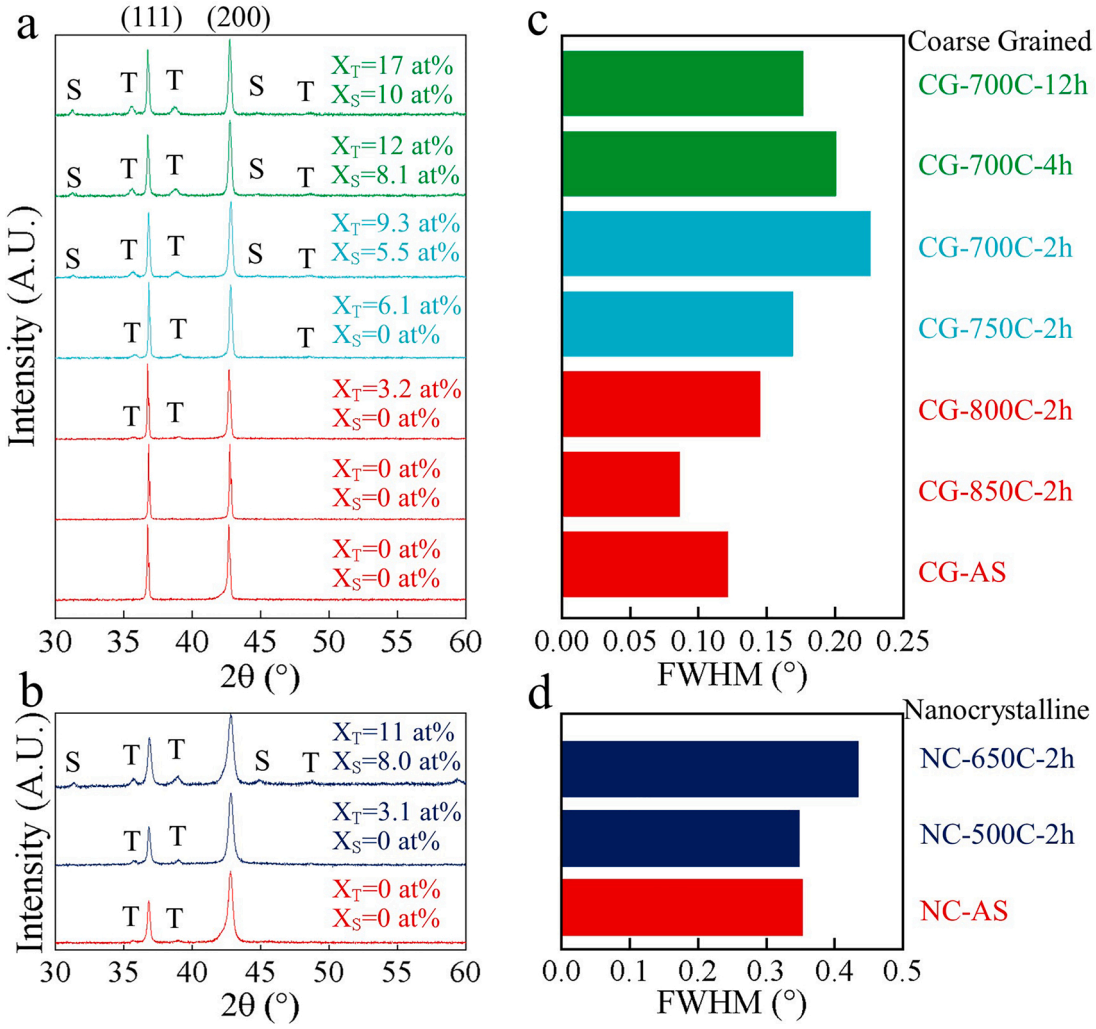

Fig. 2. Interrogation into the phase state and lattice distortion. (a-b) XRD patterns for the (a) coarse-grained and (b) nanocrystalline samples after heat treatment at the designated T_{HT} and hold times. 'T' and 'S' indicate peaks for the Cu-rich tenorite and Co-rich spinel phases, respectively. (c-d) full-width-at-half-max (FWHM) values for the (200) peak for the (c) coarse-grained and (d) nanocrystalline samples after heat treatment. The color coding designates the proposed thermodynamic driver for the observed phase state. Red corresponds to phase states that are driven by entropy. Green and light blue correspond to phase states in the coarse-grained samples that are influenced by enthalpy. Dark blue corresponds to phase states in the nanocrystalline samples that are influenced by enthalpy. (For interpretation of the references to colour in this figure legend, the reader is referred to the web version of this article.)

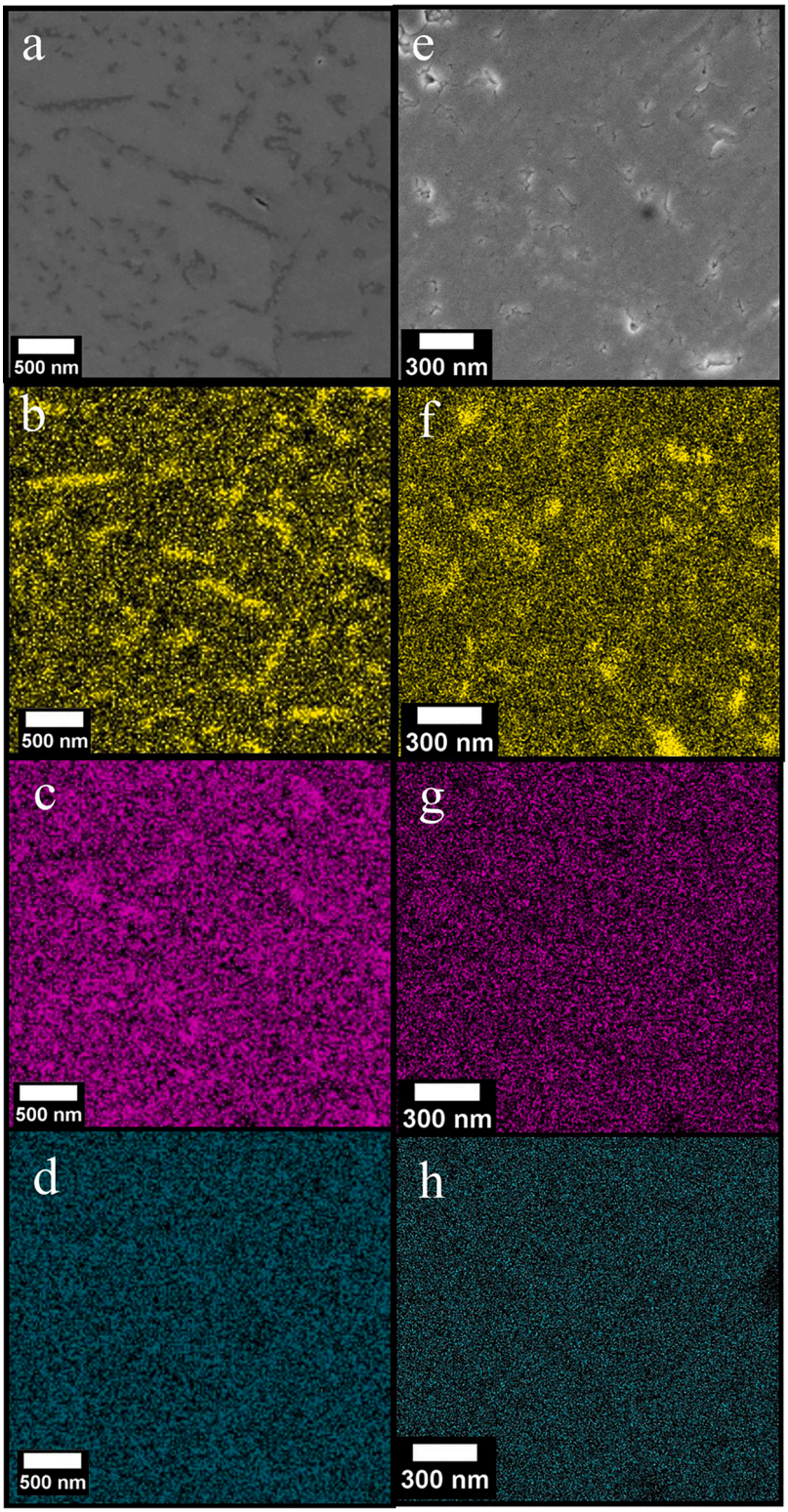

Fig. 3. Composition and morphology of the secondary phases. (a) SEM micrograph of a coarse-grained sample heat treated at 700 °C for 12 h (CG-700C-12h) and the corresponding EDS maps for (b) Cu, (c) Co, and (d) Zn, highlighting the multi-phase nature of this sample. (e) SEM micrograph of a nanocrystalline sample heat treated at 650 °C for 2 h (NC-650C-2h) and the corresponding EDS maps for (f) Cu, (g) Co, (h) Zn.

CG-700C-12h presented in Fig. 3c. Unlike the Cu-rich tenorite phase, which forms as particle and needle shaped morphologies, the Co-rich spinel phase appears as elongated particles. Like the tenorite phase, the spinel phase contains multiple cations.

Although SPS processing of the nanocrystalline samples is performed within the phase transformation temperature window, due to the short processing times, only minimal amounts of Cu-rich tenorite phase ($X_T <$ 1 at%) and no Co-rich spinel phase are observed in the as-sintered nanocrystalline sample (NC-AS) (see the XRD patterns in Fig. 2b). After heat treatment, the behavior of the nanocrystalline samples differs

from their coarse-grained counterparts. Tenorite peaks are observed in the XRD patterns after heat treatment at lower temperatures, such as T_{HT} =550 °C for 2 h (sample NC-550C-2h). Further, sample NC-650C-2h has a similar X_T to sample CG-700C-2h, which is consistent with our previous observations that consolidated nanocrystalline samples require lower temperatures and shorter times to form the tenorite phase compared to coarse-grained samples [7]. The Cu-rich tenorite phase in the nanocrystalline samples does not manifest as needles or particles (Fig. 3e). Instead, EDS analysis reveals that the Cu-rich phase emerges as individual Cu-rich grains (Fig. 3f), which is consistent with our previous observations that the Cu-rich phase encompasses entire grains in nanocrystalline samples [7]. However, the spinel phase is only observable in XRD patterns of sample NC-650C-2h (X_S = 8 at%), and is not observed by EDS in any of the nanocrystalline samples (Fig. 3g).

Analysis of the full-width-at-half-maximum (FWHM) of the XRD patterns provides information on the change in lattice distortion in the rocksalt phase [9]. The low heat-treatment temperatures used in this study are unlikely to induce meaningful grain growth in our samples, indicating that the changes in FWHM are unrelated to changes in grain size. The evolution of the FWHM in the (200) planes can be seen in Fig. 2c, with similar trends observed for all peaks. FWHM increases with decreasing T_{HT} in the coarse-grained samples until T_{HT} =700 °C. Longer hold times at T_{HT} =700 °C decrease the FWHM, while still being more than double the FWHM of the (200) peak in sample CG-850C-2h. The smallest FWHM and largest lattice constant (4.236 Å) occur in sample CG-850C-2h, while the largest FWHM and smallest lattice constant (4.228 Å) occur in sample CG-700C-2h. In contrast, for the nanocrystalline samples, increasing T_{HT} leads to an increase in the FWHM of the XRD peaks (Fig. 2d). Regardless of grain size, heat treatment of (Co, Cu,Mg,Ni,Zn)O results in a meaningful change to the FWHM of the XRD peaks associated with the rocksalt phase, indicating an evolution in the lattice distortion and the local cation electronic environment.

3.2. Electronic structure evolution

XRD patterns can track phase evolution and lattice distortion, while SEM/EDS imaging show the chemical and morphological makeup of secondary phases. However, these methods lack the resolution to examine the electronic structure of the cations, which will dictate the observed macroscopic lattice distortion. Therefore, XA spectra were acquired to probe the electronic structure of the metal cations in our samples. We consider each of the five cations individually, and the possible mechanisms that govern their behavior, in the discussion that follows.

3.2.1. Mg and Ni results

Irrespective of the experimental conditions (heat-treatment conditions, phase state, and grain size), the Mg and Ni XA spectra (not shown) remain unchanged and correspond to literature reports for these metal cations in the 2+ valence state with octahedral coordination expected in the rocksalt crystal structure. Previous EXAFS work on single-phase (Co, Cu,Mg,Ni,Zn)O suggests that Ni ions occupy an octahedral coordination with a Ni—O bond length similar to that of pure rocksalt NiO [8]. MgO is also highly stable, requiring pressures >360 GPa to transform to a non-rocksalt phase [14].

3.2.2. Cu results

The most common phases of copper oxide include CuO with a monoclinic tenorite crystal structure with Cu^{2+} ions in a planar coordination; and Cu_2O with a cubic cuprite crystal structure with Cu^{1+} ions in tetrahedral coordination. CuO can be reduced to Cu_2O under certain processing conditions [15], while ultrathin CuO films processed under specific conditions can form a tetragonal rocksalt crystal structure with Cu^{2+} ions in an elongated octahedral coordination [16]. Schematics of the octahedral, tetrahedral, and planar cation coordinations are provided in Fig. 4a–c.

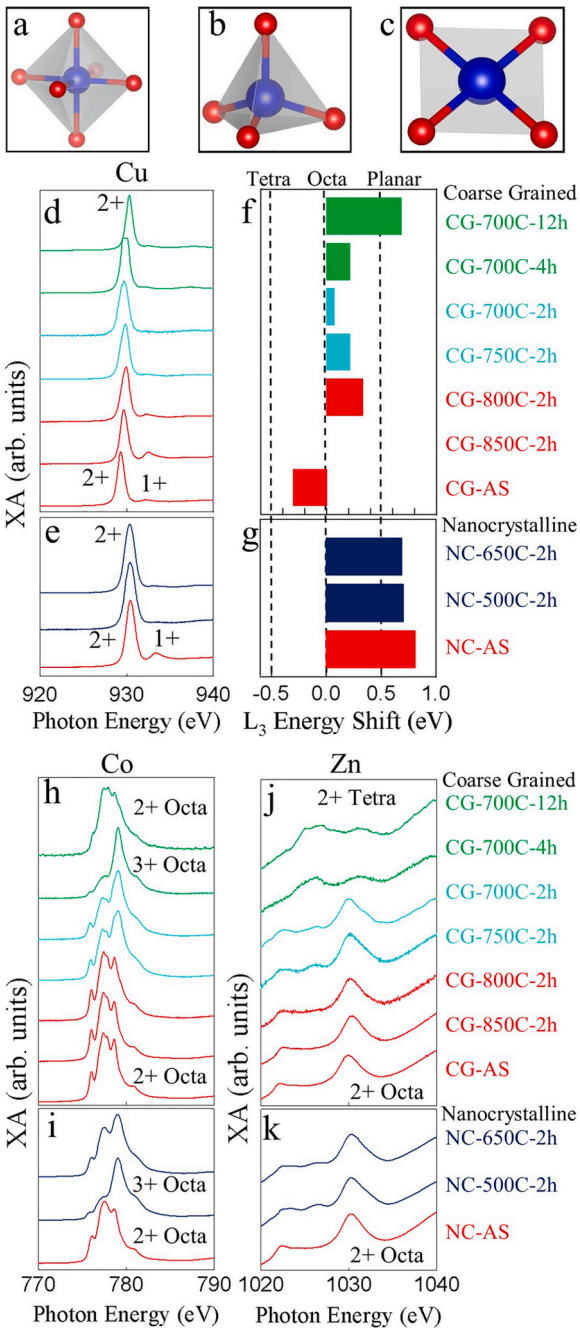

Fig. 4. Role of heat treatment and grain size on the electronic structure (valence state and cation coordination). (a-c) Example schematics of element-independent cation coordination states: (a) octahedral, (b) tetrahedral, and (c) planar. (d-e) Cu L_3 spectra for the (d) coarse-grained and (e) nanocrystalline samples after various heat treatments. (f-g) The peak energy shift (in eV) of the Cu^{2+} L_3 peak, relative to the T_{HT} =850 °C 2 h, single-phase sample (CG-850C-2h), for the (f) coarse-grained and (g) nanocrystalline samples after various heat treatments. Dashed lines indicate the expected coordination at that energy shift [17]. (h) Co and (j) Zn XA spectra for the coarse-grained samples. (i) Co and (k) Zn XA spectra for the nanocrystalline samples. The color coding designates the proposed thermodynamic driver for the observed electronic structure state. Red corresponds to electronic structure states that are driven by entropy. Green and light blue correspond to electronic structure states in the coarse-grained samples that are influenced by enthalpy. Dark blue corresponds to electronic structure states in the nanocrystalline samples that are influenced by enthalpy. (For interpretation of the references to colour in this figure legend, the reader is referred to the web version of this article.)

For samples CG-AS ($X_T = 0$ at%), CG-850C-2h ($X_T = 0$ at%), and CG-800C-2h ($X_T = 3.2$ at%), the Cu L_3-edge (Fig. 4d) exhibit a doublet feature with 2.4–2.9 eV energy separation, which can be assigned to the Cu^{2+} and Cu^{1+} states [18]. The relative intensity of the Cu^{1+} peak decreases as T_{HT} decreases, with the signal decreasing significantly for sample CG-750C-2h ($X_T = 6.1$ at%). For sample CG-700C-2h, the Cu spectra does not change significantly even though X_T increases to 9.6 at %. Similar behavior is observed in the nanocrystalline samples (Fig. 4e). Cu^{2+} and Cu^{1+} peaks are observed in the single-phase NC-AS sample, and heat treatment (samples NC-500C-2h and NC-650C-2h, with $X_T =$ 3.1 and 10.9 at%, respectively) causes the intensity of the Cu^{1+} peak to decrease significantly. Once a primarily Cu^{2+} state has been achieved, little change in the Cu XA spectra is observed with increased heat-treatment time or changes in X_T, regardless of grain size. It is important to note that the Cu^{1+} peak is present to some extent in every sample, with certain heat-treatment conditions causing its intensity to decrease significantly. The presence of a smaller Cu^{1+} peak alongside a main Cu^{2+} peak has been observed in tetragonal rocksalt CuO films [16] and other Cu-containing oxides [19], and is commonly attributed to oxygen deficiency. We expect the multi-component tenorite and spinel phases to have Cu^{2+} planar and octahedral coordinations, respectively [13].

The L-edge peak positions can be used to identify the average coordination of the Cu ion, since the peaks for Cu ions with planar and tetrahedral coordinations are shifted by 0.5 eV and −0.5 eV, respectively, compared to an octahedral Cu coordination [17]. In the current work, coarse-grain sample CG-850C-2h was selected as the starting point for analysis because the Cu^{2+} cations in single-phase (Co,Cu,Mg,Ni,Zn)O are known to have an octahedral coordination [8]. The evolution of the Cu coordination can be observed by examining the shift in the L_3 peak position. Coarse-grained samples heat treated at $T_{HT} = 700-850$ °C for 2−4 h (i.e., all CG samples except CG-700C-12h) have peak shifts ranging from 0.07 to 0.33 eV (Fig. 4f). These peak shifts fall within the expected window for an octahedral coordination with additional contributions from Jahn-Teller distortions, which can change the peak position by ~0.3 eV [17]. In contrast, sample CG-700C-12h and all three nanocrystalline samples (Fig. 4g) exhibit peak shifts >0.5 eV, indicating that the Cu^{2+} ion is primarily in planar coordination. It should be noted that in addition to the shift in the L_3 peak position, the peak width increases slightly with decreasing T_{HT}. The FWHM of the Cu^{2+} L_3 peak increases from 1.08 eV after heat treatment at 850 °C for 2 h (sample CG-850C-2h) to 1.37 eV after heat treatment at 700 °C for 2 h (sample CG-700C-2h), with the FWHM again decreasing to 1.02 eV after heat treatment at 700 °C for 12 h (sample CG-700C-12h). This trend in peak width follows the same trend as the FWHM of the XRD data and can be attributed to the convolution of the Jahn-Teller distortion, as well as the increasing amount of secondary phases and lattice distortion noted in the XRD data.

3.2.3. Co results

The most common electronic structures for Co ions include the Co^{2+} octahedral, Co^{3+} octahedral, and Co^{2+} tetrahedral coordinations, which have distinct XA spectra [20][21]. The primary cobalt oxide phase, CoO, has a rocksalt crystal structure with a Co^{2+} octahedral electronic structure. CoO will oxidize to Co_3O_4 at 600−900 °C in air [22] and then reduce back to CoO at temperatures >900 °C [23]. Co_3O_4 has a normal spinel structure with a mixture of Co^{2+} ions in a tetrahedral coordination and Co^{3+} ions in an octahedral coordination. Co ions can form normal and inverse metal-cobalt spinel phases (MCo_2O_4) with all the other cations in (Co,Cu,Mg,Ni,Zn)O, resulting in phases that contain a variety of Co electronic states. However, given that Hong et al. observed that CoO and MgO react first during the formation of single-phase equiatomic (Co,Cu,Mg,Ni,Zn)O [24], we expect to see Co^{2+} ions in an octahedral coordination in our as-sintered, single-phase samples (CG-AS and NC-AS).

The Co L_3-edge spectra for the coarse grain samples, CG-AS, CG-800C-2h and CG-850C-2h, resemble the expected Co^{2+} octahedral state found in rocksalt CoO [21] (Fig. 4h). A transformation to a Co^{3+} octahedral state begins at $T_{HT} = 700-750$ °C for 2 h, as indicated by the presence of both Co^{3+} and Co^{2+} octahedral peaks in samples CG-700C-2h and CG-750C-2h. The transformation to the predominately Co^{3+} octahedral state is complete in sample CG-700C-4h. A primarily Co^{2+} octahedral state returns as the heat-treatment time extends to 12 h in sample CG-700C-12h. A small amount of Co^{2+} tetrahedral signal can be observed as well, which we attribute to the secondary phases observed in the XRD patterns. Similar electronic structures have been observed in CoO nanotubes [25] and $NiCo_2O_4$ [26] after both had been processed in a reducing atmosphere, indicating that our phase transformation leads to some oxygen deficiency in the primary rocksalt phase. A distinct Co evolution occurs in the nanocrystalline samples (Fig. 4i). Sample NC-AS exhibits a spectrum associated with a Co^{2+} octahedral state. A complete transformation to a predominately Co^{3+} octahedral electronic structure is observed in sample NC-500C-2h ($X_T =$ 3.1 at%), while sample NC-650C-2h ($X_T = 10.9$ at% and $X_S = 8.0$ at%) has a mixture of Co^{2+} and Co^{3+} ions in octahedral coordination. Similar to the tenorite phase, the spinel phase is multi-component (see Fig. 3), and is expected to contain some amount of the other cations. For all of our samples, the majority of Co ions will reside in the primary rocksalt phase. The significant Co electronic structure evolution that we observe can therefore be attributed to both changes in the primary rocksalt phase and the formation of secondary phases.

3.2.4. Zn results

The most common crystal structures adopted by ZnO are rocksalt and wurtzite, where the Zn^{2+} ions adopt the octahedral and tetrahedral coordination, respectively, with distinct XA spectra [27]. ZnO transforms from wurtzite to rocksalt under high pressures due to a reduction in lattice dimensions [28]. Coarse-grained samples heat treated between $T_{HT} = 800-850$ °C for 2 h (i.e., samples CG-800C-2h and CG-850C-2h) have Zn L_3-edge spectra that resemble Zn^{2+} ions in octahedral coordination (Fig. 4j). Zn XA spectra indicate a transition from octahedral to tetrahedral coordination begins after 2 h at $T_{HT} = 700-750$ °C (samples CG-700C-2h and CG-750C-2h), and is complete in samples CG-700C-4h and CG-700C-12h. Like the coarse-grained samples, an octahedral coordination is observed in the as-sintered, single-phase nanocrystalline sample NC-AS (Fig. 4k), however, the transition to the tetrahedral coordination does not complete as the heat-treatment temperature and time are too low in the current study.

Since the tenorite and spinel secondary phases are both multi-component and contain some amount of Zn (see Fig. 3d and h), a portion of the Zn XA signals will originate from these secondary phases. While it is difficult to know the coordination of the Zn ions in the tenorite phase, Zn has been shown to prefer a tetrahedral coordination in spinel phases [29]. However, segregation of Zn is not observed in the EDS analysis performed on any of our samples (Fig. 3d and h), and the amount of Zn in the secondary phases is expected to be small. We therefore conclude that the evolution in the Zn ion coordination is representative of both the emergence of secondary phases as well as a transformation of the Zn ion coordination in the primary rocksalt crystal structure.

3.3. Proposed mechanisms

Entropic stabilization allows ESO systems to exhibit expanded compositional space as well as controllable phase heterogeneity (phase spectrum) [7], both of which provide ESOs with an unparalleled capacity to tailor their properties and develop new functionalities. This work shows that entropic stabilization provides a third avenue for tunability in the form of a controllable electronic structure. A schematic summarizing the electronic structure and phase evolution can be seen in Fig. 5. Although the figure is not meant to imply any direct connection between the electronic structure evolution of every cation and the at%

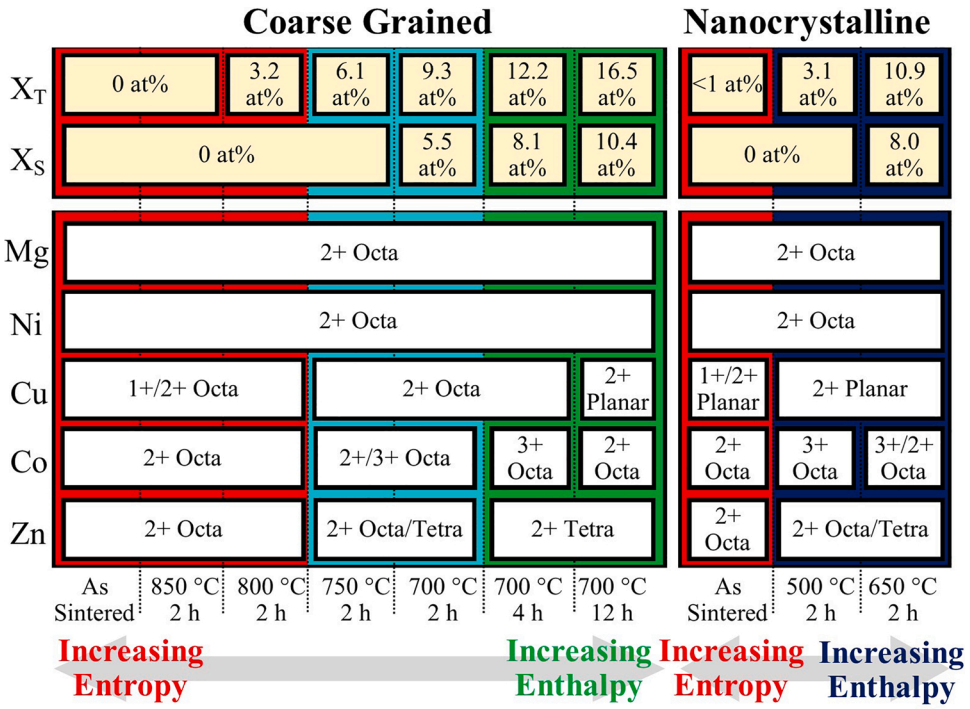

Fig. 5. Evolution of the electronic structure (valence state and cation coordination). Table summarizing the evolution in tenorite (X_T) and spinel (X_S) secondary phases as well as the evolution in electronic structure for all five cations. The corresponding heat-treatment conditions are listed at the bottom of each column. The color coding designates the proposed thermodynamic driver for the observed phase and electronic structure state. Red corresponds to electronic structure states that are driven by entropy. Green and light blue correspond to electronic structure states in the coarse-grained samples that are influenced by enthalpy. Dark blue corresponds to electronic structure states in the nanocrystalline samples that are influenced by enthalpy. (For interpretation of the references to colour in this figure legend, the reader is referred to the web version of this article.)

secondary phase (as discussed below), the amount of secondary phase(s) (i.e., X_T and X_S) can, however, be used as a proxy for the decline in metastability. We also show, for instance, that ESOs can accommodate significant changes to their electronic structure without changing crystal structures. A pattern is observed where heat treatment leads the cations to transform from six-fold to four-fold coordinated structures and from low to high valence state, both of which correspond to a decrease in the ionic radius [30]. Three of the five cations' ionic radii decrease during heat treatment and phase evolution, resulting in the observed decrease in lattice parameter and increase in structural lattice distortion with heat treatment. We hypothesize that the evolution in lattice distortion and cation electronic structure occurs due to the combined effects of three mechanisms, which are discussed below.

3.3.1. *Proposed mechanism #1*

Heat treating coarse-grained (Co,Cu,Mg,Ni,Zn)O between T_{HT} = 700−800 °C results in the formation of multi-component Cu- and Co-rich secondary phases and the oxidation of Cu^{1+} to Cu^{2+} ions and Co^{2+} to Co^{3+} ions in the primary rocksalt phase. We hypothesize that the migration of Cu and Co ions to the secondary phases leaves the rocksalt phase deficient in these cations. Even after significant secondary phase formation, however, a meaningful amount of Cu and Co remains in the primary rocksalt phase (see Fig. 3). The cations remaining in the rocksalt crystal structure adjust their electronic structures to maintain charge neutrality and long-range order, leading to the observed oxidation of the Cu and Co ions.

3.3.2. *Proposed mechanism #2*

Heat treating coarse-grained (Co,Cu,Mg,Ni,Zn)O between T_{HT} = 700−750 °C results in the transformation of the octahedrally coordinated Cu and Zn cations to planar and tetrahedral coordinations, respectively. The equilibrium coordination of CuO is planar while ZnO is tetrahedral. We propose that heat treatments below the entropic phase transformation will cause the cations in the entropy stabilized rocksalt crystal structure to transform to their enthalpy-driven electronic structures, which we propose are related to the equilibrium behavior of the binary oxides under similar conditions. Above the entropic transformation temperature, entropy stabilizes the Zn and Cu octahedral coordinations in (Co,Cu,Mg,Ni,Zn)O without requiring high pressures or special processing conditions. Temperatures within the phase spectrum window (650−850 °C) cause the enthalpy-stabilized tetrahedral and planar coordinations to be preferred. T_{HT} = 700−750 °C also falls within the temperature window for the $CoO \rightarrow Co_3O_4$ transformation and the formation temperature of various cobalt spinel phases [31]. We hypothesize that these enthalpy driven transformations will contribute to the oxidation of Co^{2+} to Co^{3+} ions in the primary rocksalt phase.

The oxidation of the Cu and Co cations in the nanocrystalline samples occurs at lower temperatures and lower X_T and X_S values than in the coarse-grained samples. The cation evolution in the nanocrystalline samples cannot be attributed solely to the segregation of secondary phases (mechanism #1) and must also be related to the competition between enthalpy- and entropy-driven electronic structures. It has been observed that decreasing the particle size of CuO nanoparticles increases the temperature required for reduction to Cu_2O [32]. Similarly, decreasing the particle size of Cu_2O nanoparticles increased the fraction of Cu^{2+} ions after synthesis [33]. These results indicate that CuO and the Cu^{2+} valence state are more stable at smaller particle sizes. CoO nanoparticles and thin films transform to Co_3O_4 and back to CoO at lower temperatures than their coarse-grained counterparts [34,35]. Similarly, the formation and decomposition temperatures of Co spinel phases depend sensitively on grain size and sample preparation [13]. Additionally, calorimetric measurements have shown that particle size does not significantly influence entropy in CoO [36] and CoO-ZnO [37]. We therefore attribute the Cu and Co coordination evolution in our nanocrystalline samples to the secondary phase formation as well as the nanocrystalline grain sizes shifting the electronic structure transformations to lower temperatures.

3.3.3. *Proposed mechanism #3*

It has been previously observed that deviating from equimolarity reduces the entropy in (Co,Cu,Mg,Ni,Zn)O, leading to the entropy-stabilized single-phase state being less stable [1]. The change in stoichiometry from mechanism #1 will result in the rocksalt phase deviating from equimolarity, reducing the entropy and driving force to maintain the metastable entropy-stabilized rocksalt phase. This reduction in entropy will exacerbate the behavior in mechanism #2. We propose that

the formation of secondary phases will decrease the entropy in ESO materials, leading to the favorability of enthalpy-driven electronic structures. Such a phenomenon could also explain why the spinel phase emerges under such a specific set of conditions. The spinel phase may lack the free energy necessary to overcome the entropy-stabilized single-phase state until the entropy of the rocksalt phase has been reduced.

3.3.4. Discussion

Mechanism #1, the segregation of the Cu-rich and Co-rich phases, will play a significant role in the electronic structure evolution. During heat treatment the rocksalt phase is unstable, leading to phase segregation. As cations diffuse out, the rocksalt phase will be depleted in Cu and Co, resulting in the rocksalt phase adjusting its electronic structure, contributing to our observed changes in the XA spectra. However, previous work by Berardan et al. shows that Cu deficient ESO does not exhibit an increase in XRD peak width or any obvious signs of lattice distortion in the crystal structure [9]. Additionally, the authors find that samples heat treated at temperatures below 600 °C do not form secondary phases, but still display a significant increase in the FWHM of the rocksalt crystal structure XRD peaks. Our heat-treated samples exhibit Cu-rich secondary phase formation, resulting in a loss of Cu in the primary rocksalt phase. The increase in FWHM of the rocksalt XRD peaks with decreasing heat-treatment temperature indicates that the observed phase segregation is not the sole driver of the lattice distortion in the rocksalt crystal structure. We therefore conclude that mechanism #2, the competition between entropy and enthalpy driven electronic structures, will partially contribute to the electronic structure state in the rocksalt phase of (Co,Cu,Mg,Ni,Zn)O. We hypothesize that all three mechanisms will play a role in the electronic structure evolution.

The influence of T_{HT} and time on the electronic structure of Cu, Zn, and Co ions can be visualized in Fig. 6. Displayed are schematics of the relevant microstructures that emerge alongside and contribute to the electronic structure evolution, derived from Fig. 3 and our previous work [7]. Mechanisms 1–3 lead to a controllable electronic structure, providing ESO materials with unparalleled design flexibility. Since electronic structure influences most functional properties, ESOs have the capability to optimize and expand their properties for a wide range of applications. (Co,Cu,Mg,Ni,Zn)O is the ideal system to demonstrate this new concept as Zn and Co represent two different styles of modifiable electronic structure design. ZnO has a Zn^{2+} tetrahedral state at ambient conditions and would be expected to have some enthalpic propensity to return to that electronic structure. Alternatively, CoO has a Co^{2+} octahedral state at room temperature, allowing it to easily integrate into the (Co,Cu,Mg,Ni,Zn)O rocksalt phase and facilitate the stabilization of the single-phase state. The conveniently located temperature windows for spinel formation and the $CoO \rightarrow Co_3O_4$ transformation give (Co,Cu,Mg,Ni,Zn)O access to an enthalpy-driven electronic structure change, while the separation of Cu and Co from the rocksalt phase provides an additional mechanism to oxidize Co^{2+} ions.

It is important to note that entropy can play a role in stabilizing inverse and random spinel crystal structures due to random occupancy on the cation sublattices [38]. Further, the degree of inversion, and thus the role of entropy, increases with increasing temperature in many spinel phases [39]. The observation of a secondary spinel phase in the heat-treated ESO samples complicates any discussion of the role of entropy and enthalpy in the phase transformation, while also leaving open the possibility that ESO materials can have additional entropy driven transformations. Our results indicate that the competition between entropy and enthalpy in ESOs is not one dimensional and is flexible enough to allow complex phase, crystal, and electronic structure transformations. Clever materials engineering will allow similar designs to be leveraged to make ESO systems with useful electronic structure transformations.

We hypothesize that similar evolutions in lattice distortion and electronic structure occur in other HEO systems. The current definition of entropy stabilization focuses on the competition between enthalpy and entropy-driven phase states. We propose that this criterion is too narrow and should expand to include the competition between electronic structures. Although less obvious than a change in phase state, an entropy-stabilized electronic structure is still a unique feature to ESOs and will greatly expand the potential for this class of materials. Additionally, we show that (Co,Cu,Mg,Ni,Zn)O has a Co-rich spinel phase that emerges under a narrow range of heat-treatment conditions, indicating that some entropic phase transformations may be difficult to observe. Our work demonstrates that entropic transformations can be subtle, and it is worthwhile to re-evaluate the entropic stability of previously examined HEO systems.

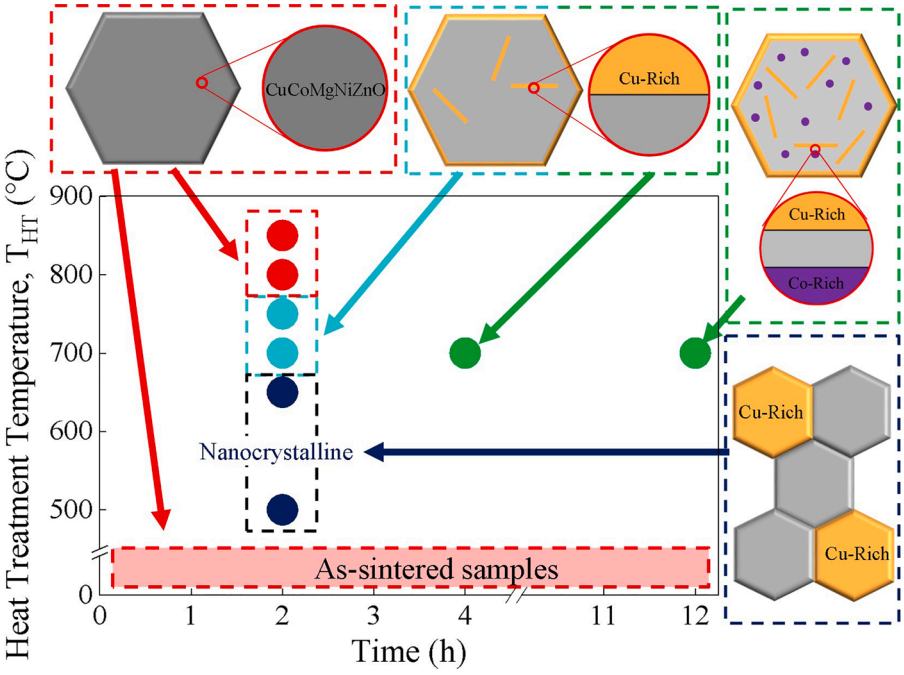

Fig. 6. T_{HT} vs hold time demonstrating the effect of heat-treatment conditions on the electronic structure. Closed circles correspond to samples measured using XA spectroscopy, with the color corresponding to the phase and electronic states from Fig. 5. Arrows connect microstructure and phase morphology schematics, derived from Fig. 3 and our previous work [7], to their relevant heat-treatment conditions. The color coding designates the proposed thermodynamic driver for the observed phase and electronic structure state. Red corresponds to states that are driven by entropy. Green and light blue correspond to states in the coarse-grained samples that are influenced by enthalpy. Dark blue corresponds to states in the nanocrystalline samples that are influenced by enthalpy. (For interpretation of the references to colour in this figure legend, the reader is referred to the web version of this article.)

4. Conclusions

The combination of XAS, XRD, SEM and EDS measurements enabled the observation of the reversible evolution in the phase state and electronic structure of (Co,Cu,Mg,Ni,Zn)O after heat treatment. Heat treatment below the entropic transformation temperature results in increased lattice distortion due to transformations to enthalpy-stabilized electronic structures. These transformations occur due to the influence of secondary phases as well as the dominance of enthalpy-driven electronic structures under those conditions. Additionally, this evolution in electronic structure was found to be influenced by grain size. Our results show that it is possible to leverage the thermodynamic competition between entropy and enthalpy in ESO materials to produce controllable lattice distortion and electronic structures. The ability to control the valence state and cation coordination will allow for the optimization of functional properties and the development of never before seen capabilities. We believe that this phenomenon exists in other HEOs, including ones that were overlooked for not exhibiting an entropy-stabilized phase. Finally, we observe the formation of a Co-rich spinel phase for the first time, which only emerges under a narrow temperature window. Our results give reason to re-evaluate previous HEO systems and the design strategies for future HEO development. The expanded compositional space, phase spectrum, and now the controllable electronic structure, available to ESOs demonstrates that this class of materials is well positioned to revolutionize nearly every category of material property.

Summary of novel conclusions

- The combination of X-ray absorption spectroscopy, X-ray diffraction, scanning electron microscopy, and energy dispersive X-ray spectroscopy measurements enabled the observation of the reversible evolution in the phase state and electronic structure of (Co,Cu,Mg,Ni,Zn)O entropy stabilized oxide after heat treatment. Heat treatment below the entropic transformation temperature results in increased lattice distortion due to transformations to enthalpy-stabilized electronic structures. Specifically, heat treatment leads Cu, Co, and Zn ions to reversibly transform from six-fold to four-fold coordinated structures and from low to high valence state.
- These transformations occur due to the influence of secondary phases as well as the dominance of enthalpy-driven electronic structures under those conditions. Additionally, this evolution in electronic structure was found to be influenced by grain size.
- Our results show that it is possible to leverage the thermodynamic competition between entropy and enthalpy in entropy stabilized oxide materials to produce controllable lattice distortion and electronic structures. The ability to control the valence state and cation coordination will allow for the optimization of functional properties and the development of never-before-seen capabilities.
- We believe that this phenomenon exists in other high entropy oxides, including ones that were overlooked for not exhibiting an entropy-stabilized phase. Our results give reason to re-evaluate previous high entropy oxide systems and the design strategies for future high entropy oxide development.

Declaration of Competing Interest

The authors report no declarations of interest.

Acknowledgements

This research used resources at the Advanced Light Source, which is a DOE Office of Science User Facility, under contract No. DE-AC02-05CH11231. XRD and SEM characterization was performed at the UC Irvine Materials Research Institute (IMRI). IC and YT acknowledge financial support from the National Science Foundation under grant DMR-1745450. ADD and JMS acknowledge financial support from the UCI Samueli School of Engineering and the National Science Foundation under award CMMI-2029966.

References

[1] C.M. Rost, E. Sachet, T. Borman, A. Moballegh, E.C. Dickey, D. Hou, J.L. Jones, S. Curtarolo, J.-P. Maria, Entropy-stabilized oxides, Nat. Commun. 6 (2015) 8485, https://doi.org/10.1038/ncomms9485.

[2] A. Sarkar, Q. Wang, A. Schiele, M.R. Chellali, S.S. Bhattacharya, D. Wang, T. Brezesinski, H. Hahn, L. Velasco, B. Breitung, High-entropy oxides: fundamental aspects and electrochemical properties, Adv. Mater. 31 (2019), 1806236, https://doi.org/10.1002/adma.201806236.

[3] D. Bérardan, S. Franger, D. Dragoe, A.K. Meena, N. Dragoe, Colossal dielectric constant in high entropy oxides, Phys. Status Solidi - Rapid Res. Lett. 10 (2016) 328–333, https://doi.org/10.1002/pssr.201600043.

[4] D. Bérardan, S. Franger, A.K. Meena, N. Dragoe, Room temperature lithium superionic conductivity in high entropy oxides, J. Mater. Chem. A 4 (2016) 9536–9541, https://doi.org/10.1039/C6TA03249D.

[5] S.H. Albedwawi, A. AlJaberi, G.N. Haidemenopoulos, K. Polychronopoulou, High entropy oxides-exploring a paradigm of promising catalysts: a review, Mater. Des. 202 (2021), 109534, https://doi.org/10.1016/j.matdes.2021.109534.

[6] A. Sarkar, L. Velasco, D. Wang, Q. Wang, G. Talasila, L. de Biasi, C. Kübel, T. Brezesinski, S.S. Bhattacharya, H. Hahn, B. Breitung, High entropy oxides for reversible energy storage, Nat. Commun. 9 (2018) 3400, https://doi.org/10.1038/s41467-018-05774-5.

[7] A.D. Dupuy, X. Wang, J.M. Schoenung, Entropic phase transformation in nanocrystalline high entropy oxides, Mater. Res. Lett. 7 (2019) 60–67, https://doi.org/10.1080/21663831.2018.1554605.

[8] C.M. Rost, Z. Rak, D.W. Brenner, J.-P. Maria, Local structure of the Mg x Ni x Co x Cu x Zn x O(x =0.2) entropy-stabilized oxide: an EXAFS study, J. Am. Ceram. Soc. 100 (2017) 2732–2738, https://doi.org/10.1111/jace.14756.

[9] D. Berardan, A.K. Meena, S. Franger, C. Herrero, N. Dragoe, Controlled Jahn-Teller distortion in (MgCoNiCuZn)O-based high entropy oxides, J. Alloys Compd. 704 (2017) 693–700, https://doi.org/10.1016/j.jallcom.2017.02.070.

[10] S. Burgess, J. Sagar, J. Holland, X. Li, F. Bauer, Ultra-low kV EDS – a new approach to improved spatial resolution, surface sensitivity, and light element compositional imaging and analysis in the SEM, Micros. Today 25 (2017) 20–29, https://doi.org/10.1017/S1551929517000013.

[11] L. Lutterotti, M. Bortolotti, G. Ischia, I. Lonardelli, H.-R. Wenk, Rietveld texture analysis from diffraction images, Z. Kristallogr. (Suppl. 26) (2007) 125–130, https://doi.org/10.1524/zksu.2007.2007.suppl_26.125.

[12] J.-S. Lee, D.A. Arena, P. Yu, C.S. Nelson, R. Fan, C.J. Kinane, S. Langridge, M. D. Rossell, R. Ramesh, C.-C. Kao, Hidden magnetic configuration in epitaxial La_{1-x} sr_x MnO_3 films, Phys. Rev. Lett. 105 (2010), 257204, https://doi.org/10.1103/PhysRevLett.105.257204.

[13] D. Klissurski, E. Uzunova, Synthesis and features of binary cobaltite spinels, J. Mater. Sci. 29 (1994) 285–293, https://doi.org/10.1007/BF01162484.

[14] R.S. McWilliams, D.K. Spaulding, J.H. Eggert, P.M. Celliers, D.G. Hicks, R.F. Smith, G.W. Collins, R. Jeanloz, Phase transformations and metallization of magnesium oxide at high pressure and temperature, Science 338 (2012) 1330–1333, https://doi.org/10.1126/science.1229450.

[15] J.A. Rodriguez, J.Y. Kim, J.C. Hanson, M. Pérez, A.I. Frenkel, Reduction of CuO in H2: in situ time-resolved XRD studies, Catal. Letters 85 (2003) 247–254, https://doi.org/10.1023/A:1022110200942.

[16] D. Samal, H. Tan, Y. Takamura, W. Siemons, J. Verbeeck, G. Van Tendeloo, E. Arenholz, C.A. Jenkins, G. Rijnders, G. Koster, Direct structural and spectroscopic investigation of ultrathin films of tetragonal CuO: six-fold coordinated copper, EPL 105 (2014), 17003, https://doi.org/10.1209/0295-5075/105/17003.

[17] K. Shimizu, H. Maeshima, H. Yoshida, A. Satsuma, T. Hattori, Ligand field effect on the chemical shift in XANES spectra of Cu(II) compounds, Phys. Chem. Chem. Phys. 3 (2001) 862–866, https://doi.org/10.1039/b007276l.

[18] Y. Wang, S. Lany, J. Ghanbaja, Y. Fagot-Revurat, Y.P. Chen, F. Soldera, D. Horwat, F. Mücklich, J.F. Pierson, Electronic structures of C u 2 O, C u 4 O 3, and CuO: a joint experimental and theoretical study, Phys. Rev. B 94 (2016), 245418, https://doi.org/10.1103/PhysRevB.94.245418.

[19] N. Nücker, E. Pellegrin, P. Schweiss, J. Fink, S.L. Molodtsov, C.T. Simmons, G. Kaindl, W. Frentrup, A. Erb, G. Müller-Vogt, Site-specific and doping-dependent electronic structure of YBa2Cu3Ox probed by O 1s and Cu 2p x-ray-absorption spectroscopy, Phys. Rev. B 51 (1995) 8529–8542, https://doi.org/10.1103/PhysRevB.51.8529.

[20] X. Long, P. Yu, N. Zhang, C. Li, X. Feng, G. Ren, S. Zheng, J. Fu, F. Cheng, X. Liu, Direct spectroscopy for probing the critical role of partial covalency in oxygen reduction reaction for cobalt-manganese spinel oxides, Nanomaterials 9 (2019) 577, https://doi.org/10.3390/nano9040577.

[21] A.M. Hibberd, H.Q. Doan, E.N. Glass, F.M.F. de Groot, C.L. Hill, T. Cuk, Co polyoxometalates and a Co_3 O $_4$ thin film investigated by L-edge X-ray absorption spectroscopy, J. Phys. Chem. C 119 (2015) 4173–4179, https://doi.org/10.1021/jp5124037.

[22] W.J. Tomlinson, A. Easterlow, Kinetics and microstructure of oxidation of CoO to Co3O4 at 700–800°C, J. Phys. Chem. Solids 46 (1985) 151–153, https://doi.org/10.1016/0022-3697(85)90211-2.

[23] G.A. El-Shobaky, I.F. Hewaidy, T. El-Nabarawy, Sintering of non-stoichiometric NiO, CoO and Co3O4 catalysts, Surf. Technol. 12 (1981) 309–315, https://doi.org/10.1016/0376-4583(81)90025-X.
[24] W. Hong, F. Chen, Q. Shen, Y. Han, W.G. Fahrenholtz, L. Zhang, Microstructural evolution and mechanical properties of (Mg,Co,Ni,Cu,Zn)O high-entropy ceramics, J. Am. Ceram. Soc. 102 (2019) 2228–2237, https://doi.org/10.1111/jace.16075.
[25] Y. Wang, K. Jiang, H. Zhang, T. Zhou, J. Wang, W. Wei, Z. Yang, X. Sun, W. Bin Cai, G. Zheng, Bio-inspired leaf-mimicking nanosheet/nanotube heterostructure as a highly efficient oxygen evolution catalyst, Adv. Sci. 2 (2015), 1500003, https://doi.org/10.1002/advs.201500003.
[26] H.-W. Chang, C.-L. Dong, Y.-R. Lu, Y.-C. Huang, C.-L. Chen, J.-L. Chen, J.-M. Chen, J.-F. Lee, Y.-C. Tsai, Ex-situ soft X-ray absorption spectroscopic investigation of NiCo2O4 annealed in different gases for hydrogen generation by electrolysis of urea, Int. J. Hydrogen Energy 44 (2019) 15771–15778, https://doi.org/10.1016/j.ijhydene.2018.10.108.
[27] T. Mizoguchi, I. Tanaka, S. Yoshioka, M. Kunisu, T. Yamamoto, W.Y. Ching, First-principles calculations of ELNES and XANES of selected wide-gap materials: dependence on crystal structure and orientation, Phys. Rev. B 70 (2004), 045103, https://doi.org/10.1103/PhysRevB.70.045103.
[28] Ü. Özgür, Y.I. Alivov, C. Liu, A. Teke, M.A. Reshchikov, S. Doğan, V. Avrutin, S.-J. Cho, H. Morkoç, A comprehensive review of ZnO materials and devices, J. Appl. Phys. 98 (2005), 041301, https://doi.org/10.1063/1.1992666.
[29] A. Navrotsky, O.J. Kleppa, The thermodynamics of cation distributions in simple spinels, J. Inorg. Nucl. Chem. 29 (1967) 2701–2714, https://doi.org/10.1016/0022-1902(67)80008-3.
[30] R.D. Shannon, Revised effective ionic radii and systematic studies of interatomic distances in halides and chalcogenides, Acta Crystallogr. Sect. A 32 (1976) 751–767, https://doi.org/10.1107/S0567739476001551.
[31] D. Darbar, M.R. Anilkumar, V. Rajagopalan, I. Bhattacharya, H.I. Elim, T. Ramakrishnappa, F.I. Ezema, R. Jose, M.V. Reddy, Studies on spinel cobaltites, MCo2O4 (M = Mn, Zn, Fe, Ni and Co) and their functional properties, Ceram. Int. 44 (2018) 4630–4639, https://doi.org/10.1016/j.ceramint.2017.12.010.
[32] J. Pike, S.-W. Chan, F. Zhang, X. Wang, J. Hanson, Formation of stable Cu2O from reduction of CuO nanoparticles, Appl. Catal. A Gen. 303 (2006) 273–277, https://doi.org/10.1016/j.apcata.2006.02.008.
[33] J. Song, P.P. Rodenbough, L. Zhang, S.-W. Chan, Size-dependent crystal properties of nanocuprite, Int. J. Appl. Ceram. Technol. 13 (2016) 389–394, https://doi.org/10.1111/ijac.12486.
[34] K.M. Nam, J.H. Shim, D.-W. Han, H.S. Kwon, Y.-M. Kang, Y. Li, H. Song, W.S. Seo, J.T. Park, Syntheses and characterization of wurtzite CoO, rocksalt CoO, and spinel Co 3 O 4 nanocrystals: their interconversion and tuning of phase and morphology, Chem. Mater. 22 (2010) 4446–4454, https://doi.org/10.1021/cm101138h.
[35] K. Biedermann, M. Gubo, L. Hammer, K. Heinz, Phases and phase transitions of hexagonal cobalt oxide films on Ir(100)-(1 × 1), J. Phys. Condens. Matter 21 (2009), 185003, https://doi.org/10.1088/0953-8984/21/18/185003.
[36] L. Wang, K. Vu, A. Navrotsky, R. Stevens, B.F. Woodfield, J. Boerio-Goates, Calorimetric study: surface energetics and the magnetic transition in nanocrystalline CoO, Chem. Mater. 16 (2004) 5394–5400, https://doi.org/10.1021/cm049040i.
[37] C. Ma, A. Navrotsky, Thermodynamics of the CoO–ZnO system at bulk and nanoscale, Chem. Mater. 24 (2012) 2311–2315, https://doi.org/10.1021/cm3005198.
[38] A. Navrotsky, O.J. Kleppa, Thermodynamics of formation of simple spinels, J. Inorg. Nucl. Chem. 30 (1968) 479–498, https://doi.org/10.1016/0022-1902(68)80475-0.
[39] A. Seko, K. Yuge, F. Oba, A. Kuwabara, I. Tanaka, Prediction of ground-state structures and order-disorder phase transitions in II-III spinel oxides: a combined cluster-expansion method and first-principles study, Phys. Rev. B 73 (2006), 184117, https://doi.org/10.1103/PhysRevB.73.184117.